Solar activity across the scales: from small-scale quiet-Sun dynamics to magnetic activity cycles

Irina N. Kitiashvili[1], Nancy N. Collins[2], Alexander G. Kosovichev[3], Nagi N. Mansour[1], Alan A. Wray[1]

[1]NASA Ames Research Center, [2]NCAR, [3]New Jersey Institute of Technology

Observations as well as numerical and theoretical models show that solar dynamics is characterized by complicated interactions and energy exchanges among different temporal and spatial scales. It reveals magnetic self-organization processes from the smallest scale magnetized vortex tubes to the global activity variation known as the solar cycle. To understand these multiscale processes and their relationships, we use a two-fold approach: 1) realistic 3D radiative MHD simulations of local dynamics together with high-resolution observations by IRIS, Hinode, and SDO; and 2) modeling of solar activity cycles by using simplified MHD dynamo models and mathematical data assimilation techniques. We present recent results of this approach, including the interpretation of observational results from NASA heliophysics missions and predictive capabilities. In particular, we discuss the links between small-scale dynamo processes in the convection zone and atmospheric dynamics, as well as an early prediction of Solar Cycle 25.

Realistic modeling of local dynamics

'SolarBox' code (Wray et al., 2015)

- ✓ 3D rectangular geometry
- ✓ Fully conservative, Fully compressible
- ✓ Fully coupled radiation solver:
  - LTE using 4 opacity-distribution-function bins
  - Ray-tracing transport by Feautrier method
  - 18 ray angular quadrature
- ✓ Non-ideal (tabular) EOS
- ✓ 4th order Padé spatial discretization
- ✓ 4th order Runge-Kutta time integration
- ✓ Turbulence models:
  - Compressible Smagorinsky model
  - Compressible Dynamics Smagorinsky mode (Germano et al., 1991; Moin et al., 1991)
  - MHD subgrid models (Balarac et al., 2010)
  - DNS+Hyperviscosity approach
- ✓ MPI parallelization (plane and pencil versions)

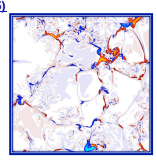

Formation of magnetic patches by turbulent dynamo action from an initial 10^{-6}G random seed field. The blue-red color scale corresponds to vertical magnetic field strengths from -300 to 300 G at the photosphere layer. A typical size of the magnetic structures is 100 to 300 km.

Basic equations

The equations are the grid-cell averaged

Conservation of mass: $\frac{\partial \rho}{\partial t} + \left(\rho u_i\right)_{,i} = 0$

Conservation of momentum: $\frac{\partial \rho u_i}{\partial t} + \left(\rho u_i u_j + P_{ij}\right)_{,j} = -\rho\phi_{,j}$

Conservation of energy:

$$\frac{\partial E}{\partial t} + \left(\begin{array}{l} Eu_i + P_{ij}u_j - \kappa T_{,i} + \\ + \left(\frac{c}{4\pi}\right)^2 \frac{1}{\sigma}\left(B_{i,j} - B_{j,i}\right)B_j + F_i^{rad} \end{array} \right)_{,i} = 0$$

with

$$P_{ij} = \left(p + \frac{2}{3}\rho u_{k,k} + \frac{1}{8\pi}B_k B_k\right)\delta_{ij} - \mu\left(u_{i,j} + u_{j,i}\right) - \frac{1}{4\pi}B_i B_j$$

Conservation of magnetic flux

$$\frac{\partial B_i}{\partial t} + \left(u_j B_i - u_i B_j - \frac{c^2}{4\pi\sigma}\left(B_{i,j} - B_{j,i}\right)\right)_{,j} = 0$$

Small-scale dynamo

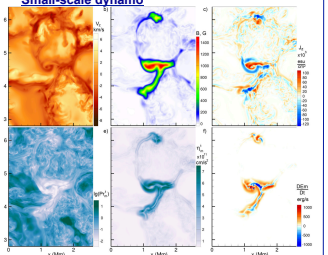

Horizontal snapshot of a fraction of the computational domain in the photosphere for: a) vertical velocity; b) magnetic field strength; c) vertical component of the electric current density; d) logarithm of the turbulent magnetic Prandtl number; e) turbulent magnetic diffusivity; and f) time-derivative of the magnetic energy density.

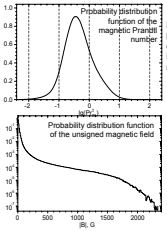

Probability distribution function of the magnetic Prandtl number

Probability distribution function of the unsigned magnetic field

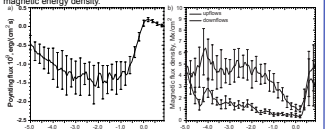

a) Mean vertical Poynting flux as a function of depth. b) Mean horizontal magnetic fluxes in up-flows (thin curve) and in down-flows (thick curve). All properties are averaged over 1 hour. Error bars show the standard deviation.

Ubiquitous small-scale eruptions

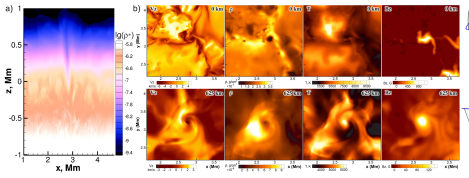

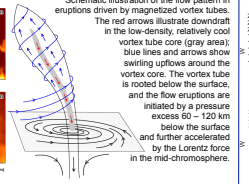

Schematic illustration of the flow pattern in eruptions driven by magnetized vortex tubes. The red arrows illustrate downdraft in the low-density, relatively cool vortex tube core (gray area); blue lines and arrows show swirling upflows around the vortex core. The vortex tube is rooted below the surface, and the flow eruptions are initiated by a pressure excess 60 – 120 km below the surface and further accelerated by the Lorentz force in the mid-chromosphere.

Panel (a) shows a vertical cut of a vortex tube that drives flow eruption and generates shock waves in the solar chromosphere. Horizontal cuts (panel (b)) show a fraction of the domain at the photosphere (top row) and at 625 km above the solar surface (bottom row) for, from left to right: vertical velocity, density, temperature, and vertical magnetic field.

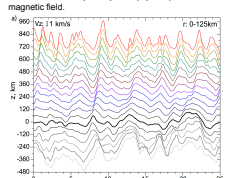

Temporal profiles of variations of the mean vertical velocity, V_z at different levels below the surface and in the atmosphere. The thick black curve shows the variations in the photosphere level. The height difference between the curves is 60 km.

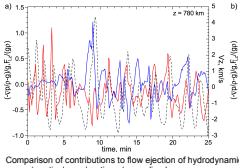

Comparison of contributions to flow ejection of hydrodynamic (red curves) and magnetic (Lorentz force, blue curves) vertical accelerations (normalized by the gravitational acceleration) at two altitudes: 780km & 300km above the photosphere. Dashed curves show the vertical velocity, V_z, given for reference at the same layers.

$$\frac{\partial \mathbf{v}}{\partial t} + (\mathbf{v}\cdot\nabla)\mathbf{v} = \boxed{\frac{\mathbf{J}\times\mathbf{B}}{c\rho}} - \frac{\nabla p}{\rho} - g$$

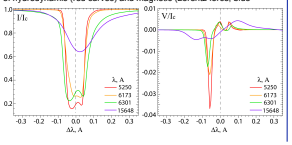

Comparison of Stokes I and V profiles, normalized by continuum intensity, for four lines during the flow eruption.

Components of the Solar Cycle Prediction Approach

Variations of solar activity are a result of complicated dynamo processes in the convection zone. We consider this phenomenon in the context of sunspot number variations, for which we have detailed observational data during the past 23 solar cycles. However, despite the known general properties of solar cycles, a reliable forecast of the 11-year sunspot number is still a problem. The main reasons for these forecasting uncertainties are imperfect dynamo models and deficiency of the necessary observational data.

To characterize the level of solar activity during systematic observations of sunspots, the relative sunspot number was introduced by Wolf (1850): **R = k(10g + n)**, where **k** is a correction factor, depending on observing conditions, **g** is the number of sunspot groups, and **n** is the number of individual sunspots.

Observations

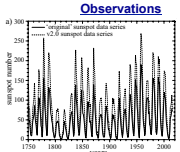

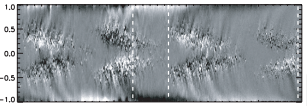

Synoptic magnetogram. The color scale is saturated at +/-15G. The white dashed lines indicate different moments of time: 1992, 1997 and 2015.

Comparison of the annual sunspot number series: the original (marked 'original' solid curve), which was used for the solar cycle 24 prediction by (Kitiashvili & Kosovichev 2008), and the 'revised' version (v2.0, Source: WDC-SILSO, Royal Observatory of Belgium, Brussels) by applying a new calibration to the historical and modern data sets (dotted curve, Clette et al. (2015) is shown in panel a).

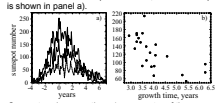

Sunspot cycle properties: a) asymmetry of the mean shape of solar cycles (dotted curve corresponds to Cycle 14, solid thick curve to Cycle 19, and thin line to Cycle 23), and b) relationship between the cycle growth time and the sunspot number maximum (Waldmeier's rule). The data are from the original sunspot number set.

Ensemble Data Assimilation

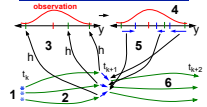

Step 1: An ensemble size of 3 model states, after the previous assimilation step.
Step 2: Each model state is independently advanced in time.
Step 3: A forward operator (h) maps each model state to an expected observation value.
Step 4: Observation increments are computed based on the relationship between the observed value and expected error vs. the distribution of expected observation values.
Step 5: The increments are regressed onto the model states and the state values adjusted.
Step 6: Each model state is advanced in time and the cycle repeats until all observations are assimilated.

Testing the Prediction Capabilities

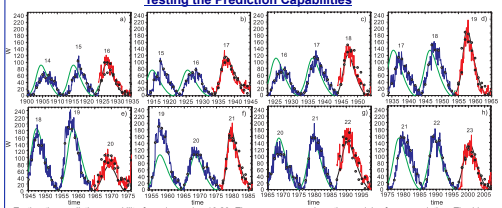

Testing the prediction capability for solar cycles 16-23. The green curves show the model reference solution. The blue curves show the best estimate of the sunspot number using the observational data (empty circles) and the model, for the previous cycles. The black curves show the model solution according to the initial conditions of the last measurement. The red curves show the prediction results.

Comparison of sunspot number predictions and estimated parameters at the solar minima

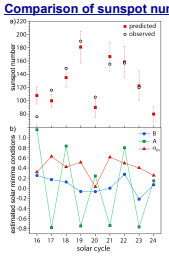

Toroidal magnetic field does not show a particular pattern and is close to zero.

Vector-potential of the poloidal field changes sign corresponding to the polar field reversal. The amplitude at the start of cycles 20 and 24 is substantially lower than during other minima.

This may correspond to the well-known correlation between the strength of the polar magnetic field and the following sunspot number (Schatten 2005; Svalgaard et al, 2005).

Magnetic helicity shows significantly better correlation with future sunspot numbers, indicating that the magnetic helicity substantially decreases prior to weak sunspot cycles.

Preliminary Analysis of Prediction Solar Cycle 25 Uncertainties

Dynamo model

Parker 1955, Kleeorin & Ruzmaikin, 1982
Kitiashvili & Kosovichev 2009, 2011

$$\frac{\partial A}{\partial t} = \alpha B + \eta\nabla^2 A \qquad \alpha_k = -(\tau/3)\langle \mathbf{u}(\nabla\times\mathbf{u})\rangle$$

$$\frac{\partial B}{\partial t} = G\frac{\partial A}{\partial z} + \eta\nabla^2 B \qquad \alpha_m = (\tau/12\pi)\langle \mathbf{h}(\nabla\times\mathbf{h})\rangle$$

$$\alpha = \alpha_k + \alpha_m$$

$$\frac{\partial \alpha_m}{\partial t} = \frac{\mu}{4\pi\rho}\left(\mathbf{B}\cdot(\nabla\times\mathbf{B}) - \frac{\alpha\mathbf{B}^2}{\eta}\right) - \frac{\alpha_m}{T_m}$$

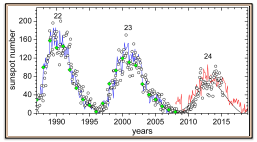

Comparison of the sunspot number prediction for Solar Cycle 24 (red curve, Kitiashvili & Kosovichev, 2008) and actual observations of monthly sunspot number. The blue curve shows the corrected dynamo solution according to annual sunspot number (green diamonds).

Data Assimilation Research Testbed

http://www.image.ucar.edu/DAReS/DART/index.php

Anderson et al., 2009; Anderson & Collins 2007

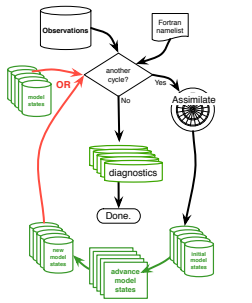

Previous experience and tests have shown that the EnKF procedure based on the dynamo model and sunspot number measurements has good predictive capabilities for estimating future solar activity in a time range from 7 - 8 years to a whole solar cycle. However, our attempts to make predictions for a period longer than one cycle often fail due to accumulation of errors. In this section, I consider in more detail the possibility of early forecasts of sunspot cycles and present an initial estimate for Cycle 25.

Early estimation of properties of Solar Cycle 25
for sunspot number version 2.0.
Panel a) shows two predictions for Cycle 25:
1) prediction obtained for observations that include the sunspot number data up to the solar minimum in 2008 (green curve);
2) prediction obtained using all currently available observations up to 2015 (red curve).
Blue curve shows the best EnKF estimates of the previous cycles based on the dynamo model and all available sunspot observation (red circles).
Panel b) shows the model errors of toroidal magnetic field variations using observations made up to 2008.
Panel c) shows these errors for the case when all available data up to 2015 are used.

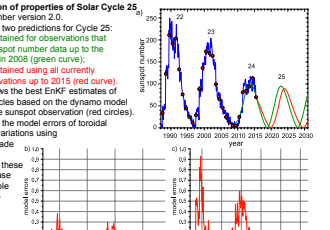

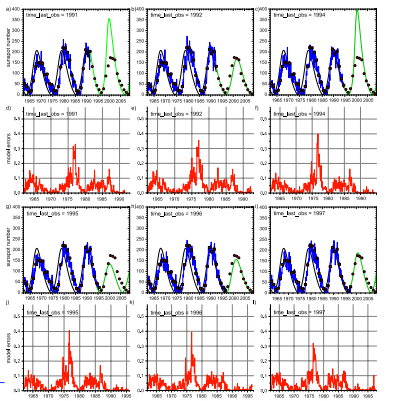

Simulated test predictions of Cycle 23 using the v2.0 annual sunspot number series. Panels *a-c* and *g-i* show Cycle 23 estimates (green curves) for the last observing times indicated in the figure panels. Black curves show the initial periodic solution obtained from the dynamo equations; red circles show the annual sunspot number. The blue curves show the best EnKF estimate of the model variations. Panels *d-f* and *j-l* show toroidal magnetic field errors of the model for each data assimilation case.

Conclusions

1. We have developed a relatively simple non-linear mean-field dynamo model, which nevertheless can describe the essential general properties of the cycles and the observed sunspot number series (such as Waldmeier's rule). Combined with the data assimilation approach, this model provides reasonable estimates for the strengths of the following solar cycles. In particular, the prediction of Cycle 24, calculated and published in 2008, is holding up quite well so far.

2. The initial prediction of Cycle 25 shows that this cycle will start in about 2019 – 2020 and reach maximum in 2023 - 2024, and the mean sunspot number at the maximum will be ~90 (for the v2.0 sunspot number series) with an estimated error of ~15%.

3. We performed 3D radiative MHD simulations taking into account all essential physics and employing sub-grid-scale turbulence models. Our numerical simulations reproduce the local dynamo process that is responsible for the quiet-Sun magnetic field. The local dynamo operates in the near-surface layers and provides a Poynting flux sufficient to heat the chromosphere and corona.

4. The small-scale dynamics is not easily observed in broad-band images even with high spatial resolution. We examined four lines (5250A, 6173A, 6301A' and 15648A) for studying the temporal evolution of Stokes profiles during a small-scale flow eruption in a weak magnetic field region. The synthetic Stokes profiles reveal interesting variations in the form of 'running-wave' perturbations across the line with time, reflecting the bidirectional flow dynamics of the eruptions. The Stokes images show ubiquitous small-scale elongated structures, which originate in the photosphere, and some of them can be identified as ultrafine loops above the granulation. In addition to the complex and dynamic Stokes I profiles, we found increasing linear polarization during the flow eruptions, which can be detectable with Hinode SP. More detailed studies are required to develop more precise and quantitative spectro-polarimetric diagnostics based on radiative MHD simulations.

References

Anderson J. 2009. Bulletin of the American Meteorological Society, 90, 1283
Anderson J.L., Collins N. 2007. Journal of Atmospheric and Oceanic Technology, 24, 1452
Balarac G., Kosovichev A. G., Brugière O., Wray A. A., Mansour N. N. 2010. ArXiV: 1010.5759.
Clette, F., Svalgaard, L., Vaquero, J. M., & Cliver, E. W. 2015. Space Sciences Ser. of ISSI, Vol. 53, 35
Eversen G. 2007. Data Assimilation. Springer
Feautrier P. 1969. In Proc. "Theory and Observation of Normal Stellar Atmospheres", Ed. Gingerich O., p. 231
Germano M., Piomelli U., Moin P., Cabot W.H. 1991. Physics of Fluids 3, 1760-1765
Kalman R.E. 1960. Problems. J. Basic. Eng., 82, series D, 35-45
Kitiashvili I. N., Kosovichev A. G. 2008. ApJ, 688, L49-L52
Kitiashvili I.N., Kosovichev A.G. 2009. Geophys. Astrophys. Fluid Dyn., 103, 53-68
Kitiashvili I.N., Kosovichev A.G. 2011. Lecture Notes in Physics, Vol. 832
Kitiashvili I. N., Kosovichev A. G., Mansour N. N., Wray A. A. 2015. ApJ 809, 84
Kitiashvili I.N. 2016. ApJ, 831, 15
Kleeorin N.I., Ruzmaikin A.A. 1982. Magnetohydrodynamics, 18, 116
Moin P., Squires K., Cabot W., Lee S. 1991. Physics of Fluids 3, 2746-2757
Parker E.N. 1955. ApJ, 122, 293
Schatten K. 2005. Geophysical Research Letters, Vol. 32, CiteID L21106
Svalgaard L., Cliver E.W., Kamide Y. 2005. ASP Conf. Series, Vol. 346, p.401
Wolf, R. 1850. Astronomische Mitteilungen der Eidgen. oeaischen Sternwarte Zurich, 1, 15
Wray A.A., Bensassi K., Kitiashvili I. N., Mansour N. N., Kosovichev A. G. 2015. ArXiV: 1507.07999